



Current variability of the Kuroshio near the separation point from the western boundary

S. Itoh¹ and T. Sugimoto²

Received 9 December 2007; revised 30 June 2008; accepted 22 September 2008; published 26 November 2008.

[1] Direct current measurements were conducted from April 2003 to March 2004 to investigate the current variability of the Kuroshio near the separation point from the western boundary. During the study period, the main stream of the Kuroshio flowed northeastward in the upper layer slightly offshore from the array of four mooring systems, while a southwestward current was observed in the intermediate layer on the coastal side of the array. Analyses based on the velocity and temperature measurement of the mooring meter array revealed eddy-to-mean kinetic and mean-to-eddy potential energy conversion in both the upper and intermediate layers. Downstream-propagating waves detected as significant extended empirical orthogonal functions (EEOFs) are predominant over velocity fluctuations of periods shorter than 50 days, explaining 67% of the total variance. The five apparent wave groups have periods of 7–18 days, wavelengths of 220–380 km, and phase velocities of 22–30 cm s⁻¹, respectively, similar to the values reported in previous studies of upstream regions. Although the phase velocity at a given wavelength in the Kuroshio is lower than that in the Gulf Stream, the dispersion tendency (i.e., that phase velocity increases with decreasing period and wavelength) is the same for both currents. The relatively low phase velocity of the Kuroshio is considered to reflect its relatively low background velocity. Data regarding growth rate, vertical phase lags, and energetics suggest that kinetic energy in this region is transferred from small to large scales mainly via eddies resulting from baroclinic instability, which is possibly related to synoptic-scale path variability and the penetration of areas of high kinetic energy into the Kuroshio Extension.

Citation: Itoh, S., and T. Sugimoto (2008), Current variability of the Kuroshio near the separation point from the western boundary, *J. Geophys. Res.*, 113, C11020, doi:10.1029/2007JC004682.

1. Introduction

[2] The Kuroshio current separates from the southeastern shelf edge off Boso Peninsula, Japan, flowing eastward as the Kuroshio Extension (Figure 1). Meso-scale wave-like meanders are commonly observed propagating downstream along the northern frontal area of the current system. Such meanders generally occur in western boundary current systems such as the Gulf Stream, and their propagation and temporal evolution have large impacts on the local hydrography, cross-frontal water mass exchange, and primary production via the supply of nutrient-rich water from lower layers. The Kuroshio current system, extending from the East China Sea to the Kuroshio Extension, has been frequently observed using satellite infrared images, successive hydrographic observations, and moored current meters.

[3] In the East China Sea, where the Kuroshio flows along the continental shelf, downstream-propagating meanders

show typical periods of 7–20 days, wavelengths of 100–350 km, and downstream phase velocities of 15–30 cm s⁻¹ [Sugimoto *et al.*, 1988; Qiu *et al.*, 1990; James *et al.*, 1999]. The meanders commonly develop into extended tongue-like bodies of warm water, entraining cold shelf water to form cyclonic eddies [Yanagi *et al.*, 1998]. The phase velocity in this region increases with decreasing period and wavelength [James *et al.*, 1999]. In the Tokara Strait, however, where the Kuroshio exits the East China Sea and enters the waters of southern Japan, these frontal disturbances are confined to the northern periphery of the stream [Feng *et al.*, 2000], even though they influence the meridional shift in the current axis within the strait [Qiu *et al.*, 1990]. Frontal disturbances are also observed in the southern area of Japan, north of the Tokara Strait. Kimura and Sugimoto [1993] carried out current measurements of the Kuroshio off Cape Shiono Misaki, and found dominant periodic fluctuations with periods of 5–8, 10–12, and 17–19 days, and wavelengths of 100, 200, and 400 km, all having phase velocities of about 20 cm s⁻¹. Unlike the waves observed by James *et al.* [1999] in the East China Sea, the estimated phase velocity was not lower for larger-scale waves, although this finding may reflect the inclusion of waves in the two short-period bands that the authors regarded as small-scale plumes from the main

¹Fisheries Environmental Oceanography Group, Ocean Research Institute, University of Tokyo, Tokyo, Japan.

²Ocean Research Institute, School of Marine Science and Technology, Tokai University, Shizuoka, Japan.

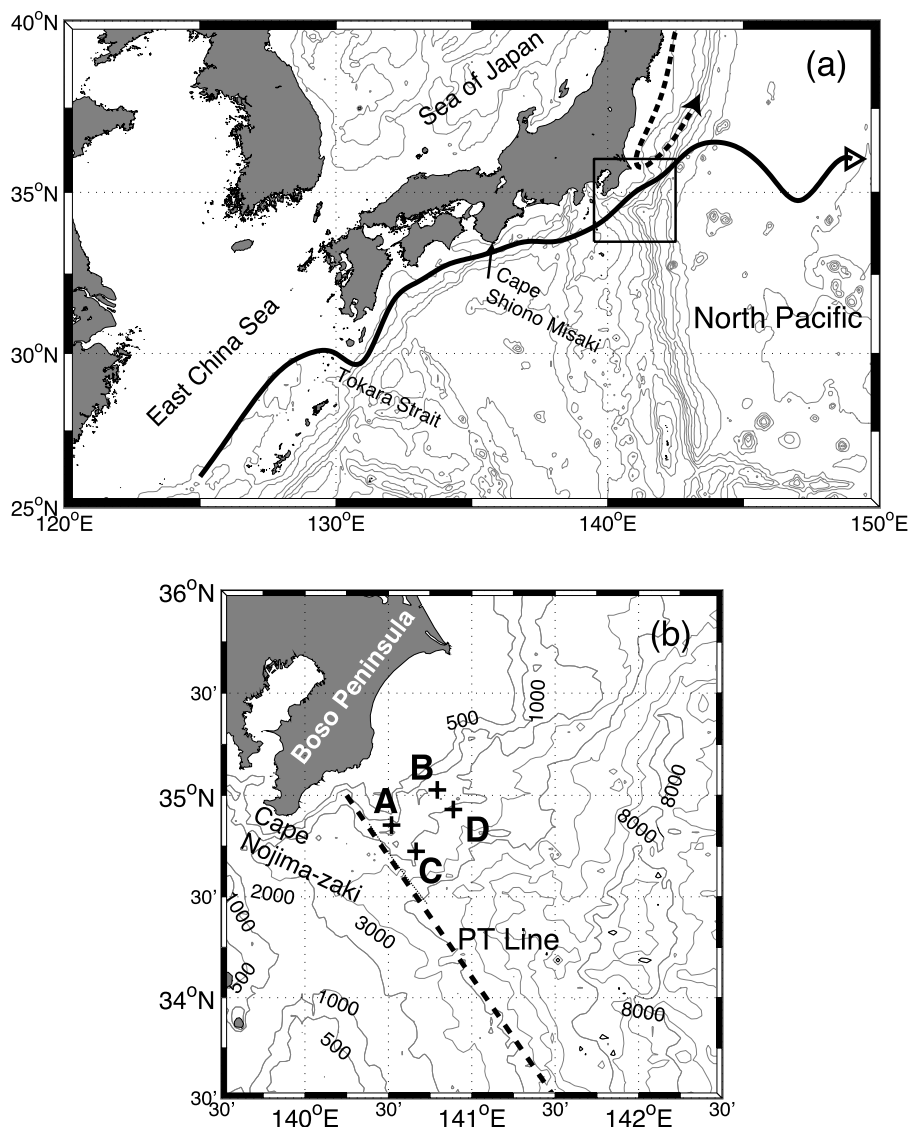


Figure 1. (a) Maps of the Kuroshio current system. (b) Maps of the locations of mooring deployments and the JMA survey line in the area where the Kuroshio diverges from the western boundary. The square in Figure 1a outlines the area shown in Figure 1b. The thick solid line and thick dashed line in Figure 1a indicate the typical path of the Kuroshio and the coastal intrusion of the Oyashio during the observation period, and crosses and the dashed line in Figure 1b indicate the mooring deployment sites and the PT line monitored by the JMA, respectively. The contour interval for isobaths is 500 m. See text for details of hydrographic observations.

stream. For two analyzed waves with periods of 17 and 19 days, the former had a longer wavelength and higher phase velocity than the latter. Similar periodic fluctuations with a period of about 20 days have been widely observed in this region, while the amplitudes depend on the synoptic-scale path of the Kuroshio [Kasai *et al.*, 1993; Kimura and Sugimoto, 2000]. In areas where the stream of the Kuroshio is detached from the coast, meanders increase in scale, warm water intrudes into the coastal area, and cyclonic eddies form with cores of cold coastal water [Kimura *et al.*, 1997].

[4] Thus the period, wavelength, and phase velocity of frontal waves in the Kuroshio along the continental shelf range from 5 to 20 days, 100 to 400 km, and 14 to 30 cm s^{-1} , respectively. Although meanders with similar wavelengths propagate downstream along the Gulf Stream in areas

upstream of Cape Hatteras (the separation point), their phase velocities are 40–70 cm s^{-1} [Brooks and Bane, 1981; Lee and Atkinson, 1983], about two to three times higher than those observed in the Kuroshio current system. The results of numerical experiments indicate that this discrepancy reflects the greater shelf depth and lesser volume transport of the Kuroshio compared with the Gulf Stream [Qiu *et al.*, 1991; James *et al.*, 1999].

[5] Contrasting wave characteristics are not only found between different current systems but also within the Gulf Stream itself, especially between those areas upstream and downstream of Cape Hatteras. For example, the amplitudes of long-period waves are higher in the downstream area, even though the wavelengths are the same in upstream and downstream areas [Watts and Johns, 1982; Tracey and Watts,

Table 1. Information on Observation Periods, Pressures, Instruments Used, and Equipped Sensors of Deployed Current Meters^a

CM	Start	End	Pressure (db)	Instrument	Sensor
A1	25 April 2003	14 January 2004	250	RCM9	VTP
B1	28 April 2003	18 March 2004	300	RCM9	VTP
C1	25 April 2003	27 August 2003	340	RCM9	VTP
D1	28 April 2003	19 March 2004	290	RCM9	VTP
A2	25 April 2003	18 March 2004	650	RCM7	VT
B2	28 April 2003	18 March 2004	710	RCM7	VT
C2	25 April 2003	11 December 2003	740	RCM7	VT
D2	28 April 2003	19 March 2004	690	RCM9	VTP
C3	25 April 2003	17 March 2004	1250	ACL-8M	VT
D3	N/A	N/A	1210	ACL-8M	VT

^aV, T, and P in the sensor column indicate velocity, temperature, and pressure, respectively. The unit db in the column of depth indicates decibar.

1986; Savidge, 2004]. This change in amplitude has been explained in terms of both barotropic and baroclinic processes [Savidge, 2004]. Although relatively low phase velocities at long wavelengths are a common feature of both the Gulf Stream and the East China Sea, they do not explain all of the observed downstream decrease in phase velocity, as the phase velocity for a given wavelength is smaller in the area from 74°W to 72°W [Tracey and Watts, 1986] than that from 75°W to 74°W [Savidge, 2004].

[6] The separation point of the Kuroshio current system is marked by an downstream increase in the scale of horizontal variability. Bernstein and White [1977] used Expendable Bathy-Thermograph (XBT) data to investigate the spatial wavenumber spectrum of temperature at 300 m depth, and found a spectral peak near 1000 km in the region west of 170°E. A quasi-stationary standing meander with crests at 144°E and 150° E has a major influence on the variability at this scale [Kawai, 1972; Mizuno and White, 1983; Tatebe and Yasuda, 2001]. Towed conductivity-temperature-depth system (CTD) observations along this meander have also revealed smaller-scale waves, with an apparent wavelength scale of 100 km, in the layer between 26.6 and 26.9 σ_θ [Kouketsu et al., 2005], corresponding to the core depth of North Pacific Intermediate Water (NPIW). The amplitudes of the waves increase downstream, and they possibly play a significant role in the intrusion of NPIW into the subtropical gyre. The three-dimensional structure of these frontal waves was further investigated by Kouketsu et al. [2007], who reported wavelengths and phase velocities of about 200 km and 20–30 cm s^{-1} , respectively; fluctuations in the upper layer preceded the intermediate-depth wave by about 1/4 of a wavelength, suggesting that the waves are baroclinically unstable; however, details of the processes of wave amplification and phase velocity transition are poorly understood because of a lack of observation data in areas near the separation point. To address this shortcoming, in the present study we undertook direct current measurements near the point at which the Kuroshio diverges from the continental shelf. These data are then analyzed using hydrographic data across the Kuroshio in this area, as observed by the Japan Meteorological Agency.

2. Data and Methods

2.1. Mooring and Hydrographic Observations

[7] Mooring systems were deployed in April 2003 from aboard the R/V *Tansei-Maru* of the Ocean Research Insti-

tute (ORI) of the University of Tokyo, Japan. The systems were deployed at four sites (A–D) off Boso Peninsula, close to the separation point of the Kuroshio (Figure 1b). The array outlined a rectangle of 30 \times 15 nautical miles (56 km \times 28 km), with the long side of the rectangle oriented parallel to the shelf isobaths. Note, however, that mooring station D was shifted slightly shoreward to ensure that it was deployed at the same depth as that of station C. The locations of the mooring stations relative to the Kuroshio were monitored in terms of the distance and direction of the Kuroshio axis from Cape Nojima-zaki, the southernmost point of Boso Peninsula, as reported weekly by the Japan Coast Guard [Japan Coast Guard, 2003, 2004]. Each mooring system was equipped with two or three current meters (Alec ACL-8M, or Aanderaa RCM-9 or RCM-7 meters) that recorded horizontal velocity, temperature, and pressure (pressure was recorded by meters A1, B1, C1, D1, and D2) at depths of approximately 300, 700, and 1200 m (Table 1). The mooring systems were retrieved in March 2004 during a cruise aboard the R/V *Hakuho-maru* of ORI. Data were successfully collected by the current meters over periods of between 4 and 11 months, except for the current meter installed at 1200 m depth at mooring site D, which worked for less than 1 day because of battery problems.

[8] The Japan Meteorological Agency (JMA) has carried out seasonal hydrographic observations across the Kuroshio off Boso peninsula since 1972. The observation line monitored by the JMA, termed the PT line, runs southwest of the mooring sites of the present study, parallel to a line through moorings A and C (Figure 1b). As part of the present study, we analyzed the across-shelf structure of temperature, salinity, and potential density observed in April, June, and October of 2003 during the period of mooring observations. Long-term records collected from 1972 to 2004 were also considered in estimating the mean fields.

2.2. Data Processing and Analyses

[9] Velocity, temperature, and pressure records obtained at 1-hour intervals were filtered by a 5th-order 36-hour Butterworth low-pass filter and subsampled at 6-hour intervals. Because the mooring systems were deployed near the jet of the Kuroshio, the instruments were forced downward, with their depths fluctuating by an order of 100 m. Three of the current meters installed at intermediate depths were not equipped with pressure sensors; consequently, pressure was approximated based on temperature records, whose vertical gradients are far larger in this area than horizontal gradients. Having determined a linear regression relation between temperature and pressure for D2, we used the obtained relation to calculate pressure data for A2, B2, and C2 based on the temperature records. The data at standard pressures of 324 and 757 decibar (db)(the mean pressures recorded by the upper and intermediate current meters), were then obtained by vertical linear interpolation or extrapolation. These two depths (pressure levels) and the layer at which C3 was installed are hereafter referred to as the upper, intermediate, and lower layers, respectively. Interpolation and extrapolation were not applied for data recorded at C3 in the lower layer. Processed temperature data were obtained only at site D, where both pressure and temperature sensors were installed at the depths of both the upper and intermediate layers.

[10] The energetics of the upper and intermediate layers are examined using these processed data from all sensors except C1 and C2, which recorded data only over particularly short intervals (Table 1). The barotropic and baroclinic energy conversion rates between the eddy and mean fields were defined as follows [Brooks and Niiler, 1977; Dewar and Bane, 1989]:

$$\text{Barotropic: } -\overline{u'u'} \frac{\partial \bar{u}}{\partial x} - \overline{u'v'} \left(\frac{\partial \bar{u}}{\partial y} + \frac{\partial \bar{v}}{\partial x} \right) - \overline{v'v'} \frac{\partial \bar{v}}{\partial y}, \quad (1)$$

$$\text{Baroclinic: } -\frac{g}{\rho_0} \overline{u'\rho'} \frac{\partial \bar{\rho}}{\partial x} \left| \frac{\partial \bar{\rho}}{\partial z} \right|^{-1} - \frac{g}{\rho_0} \overline{v'\rho'} \frac{\partial \bar{\rho}}{\partial y} \left| \frac{\partial \bar{\rho}}{\partial z} \right|^{-1}, \quad (2)$$

where primes and overbars denote anomalous and time-averaged parts, respectively. In this formulation, negative (positive) values indicate energy transfer from the eddy (mean) to the mean (eddy) field. In obtaining the barotropic conversion rates, $\overline{u'u'}$, $\overline{u'v'}$, and $\overline{v'v'}$ calculated for each of the three sites are first averaged and then multiplied by $\partial \bar{u}/\partial x$, $\partial \bar{u}/\partial y + \partial \bar{v}/\partial x$, and $\partial \bar{v}/\partial y$, as calculated using the mean velocity of the three sites; the three products are then summed. For the baroclinic conversion rate, we assume that the mean density gradient across the shelf is greater than that along the shelf, and only the cross-shelf component is used in our calculations. The cross-shelf density flux $\overline{v'_{cross}\rho'}$ is approximated based on velocity and temperature data. Density is approximated using temperature data at site D and $\rho \simeq \rho_0 (1 - \alpha_0 T')$, where $\alpha_0 = 0.17$; the cross-shelf density flux $\overline{v'_{cross}\rho'}$ is then estimated and multiplied by the mean cross-shelf density gradient $\partial \bar{\rho}/\partial y_{cross}$ and divided by the mean vertical density gradient $|\partial \bar{\rho}/\partial z|$, as estimated from the three surveys (April, June, and October 2003) undertaken by the JMA along the PT line during the observational period. Standard errors of the barotropic and baroclinic terms are estimated using the effective degrees of freedom (the minimum is used in combining multiple terms), considering the propagation of errors of correlated variables [Emery and Thomson, 2001].

[11] We performed an extended empirical orthogonal function (EEOF) analysis [Weare and Nasstrom, 1982] of the six current meter records that provide data over a relatively long period (A1, B1, D1, A2, B2, and D2). EEOF analysis is different from ordinary EOF analysis in that it uses multiple sets of lagged time series for one location rather than a single non-lagged time series. It is therefore able to extract propagating variability and its spatial structure [Miller, 1997; Nagano and Kawabe, 2005]. We employed the real-vector method [Kaihatu et al., 1998], which regards two velocity vector components as variables instead of the real and imaginary parts of a single complex variable, because the correlation between these two components plays a major role in processes of barotropic energy conversion. In obtaining EEOFs, velocity fluctuations with periods shorter than 50 days and that cover periods of frontal variability observed in previous studies were first extracted using a 5th-order Butterworth filter. The lagged time series of along- and cross-shelf velocity components, $u_i(t + \delta)$ and $v_i(t + \delta)$, were then considered, where $i = 1, 2, \dots, 6$ and $\delta = 0, 1, \dots, 50$ days, respectively, denote each

current meter and lags. EEOFs were calculated as eigen vectors of a covariance matrix \mathbf{C} of these time series ($2 \times 6 \times 51 = 612$ series):

$$\mathbf{C}W_k = \mu_k W_k \quad (3)$$

$$W_k = (U_{i=1,\delta=0,k}, U_{i=2,\delta=0,k}, \dots, U_{i=6,\delta=0,k}, U_{i=1,\delta=1,k}, \dots, U_{i=6,\delta=50,k}, \dots, V_{i=1,\delta=0,k}, V_{i=2,\delta=0,k}, \dots, V_{i=6,\delta=0,k}, V_{i=1,\delta=1,k}, \dots, V_{i=6,\delta=50,k}), \quad (4)$$

where the subscript k denotes the k -th EEOF, and $U_{i,\delta,k}$ and $V_{i,\delta,k}$ denote the k -th EEOF amplitudes of the two velocity components at time $t = t + \delta$ at the location of i -th current meter. The contribution of the k -th EEOF to the total variance can be written as $\mu_k / \sum_k \mu_k$. The dominant EEOFs can therefore be used to express the wave propagation pattern for periods of less than 50 days observed at the six current meter locations. The time coefficients of the k -th EEOF, which are used in the spectral analysis, are written as

$$\tau_k(t) = \sum_{\delta=0}^{50} \sum_{i=1}^6 [U_{i,\delta,k} u_{i,\delta}(t) + V_{i,\delta,k} v_{i,\delta}(t)]. \quad (5)$$

Significant EEOFs are selected based on Selection Rule N [Preisendorfer, 1988].

[12] The power spectral density is estimated for these time coefficient via FFT based on Welch's method [Welch, 1967]. The frequencies of the dominant energy are specified via the variance-preserving power spectral density, which is a product of an ordinary power spectral density multiplied by frequency [Emery and Thomson, 2001]. Wavelengths and phase velocities are calculated as described by Watts and Johns [1982], with the dominant frequencies and phase lags estimated by spatial cross-correlation between the spatial components of each EEOF. The growth rates of wave amplitudes are defined as

$$\sigma = C_p \ln(V_D/V_U)/\Delta l \quad (6)$$

where C_p , V_D , V_U , and Δl denote the phase velocity, the mean velocity magnitudes of the downstream and upstream stations, and the distances between these stations, respectively. This formulation is equivalent to the spectral expression given by Watts and Johns [1982]. Because of the complexity of the wave structures, detailed formulations are provided in the next section.

3. Results

3.1. Mean Field, Energetics, and Hydrography

[13] Figure 2 shows time series of processed current velocities at standard depths of 324 and 757 db. The basic statistics of the flows are listed in Table 2, and mean velocity vectors and standard deviation ellipses are shown in Figure 3. In the upper layer, a northeastward component, which apparently expresses a part of the Kuroshio, was dominant throughout the observational period at all four sites, while a southward or westward component in the intermediate layer was commonly observed in late June,

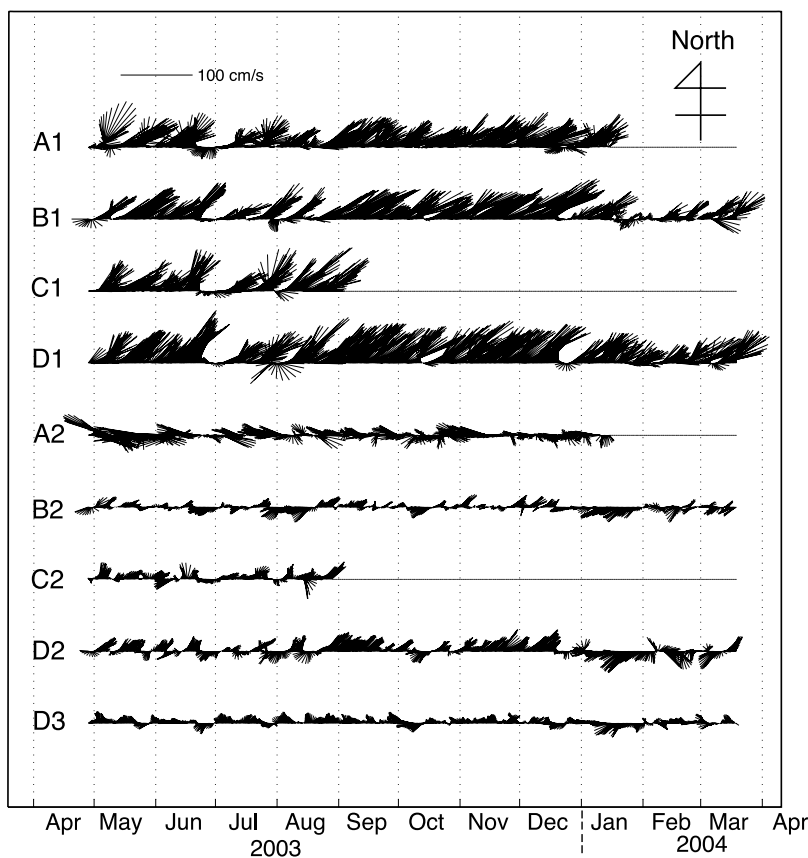


Figure 2. Stick diagrams of the current velocities and directions recorded by 10 current meters deployed in the present study. North is to the top of the page.

early August, and late December. The mean velocities were $35\text{--}45\text{ cm s}^{-1}$ toward $51\text{--}60^\circ$. The standard deviations are smaller than the mean velocities, indicating that mean kinetic energy was larger than eddy kinetic energy. In the intermediate layer, mean northeastward flows of about $6\text{--}7\text{ cm s}^{-1}$ were still recognized at the offshore sites of C2 and D2, whereas mean flows at the coastal sites were in the opposite direction to those in the upper layer (relative to the coast). Although the intermediate layer mean flows are smaller than the standard deviations at all four sites, the offshore northeastward flows and the southwestward flow at A2 are statistically significant. Because southward intrusions of cold Oyashio water from the western subarctic gyre (the Oyashio intrusion, Figure 1) were often observed in areas close to the mooring sites during 2003 and 2004 [Japan Meteorological Agency, 2005], the southwestward flow within the intermediate layer at mooring site A, where the bottom slope is steep compared with that at mooring site B, is attributable to part of this intrusion.

[14] Table 3 shows the energy conversion rates calculated using equations (1) and (2). The barotropic energy conversion rates were negative, whereas the baroclinic rates were positive, indicating that in both the upper and intermediate layers there occurred transfers of kinetic energy from the eddy field to the mean field and transfers of potential energy from the mean field to the eddy field.

[15] The lower layer at D3 showed a mean northwestward flow along the local isobaths (Figure 3), as also recorded in

the coastal part of the intermediate layer at A2 and B2; variations in flow within the lower layer were relatively isotropic.

[16] Figure 4 shows sections of temperature, salinity, and potential density along the PT line monitored by the JMA. Subtropical mode water characterized by temperatures of 18 to 19°C , salinity of 34.5 to 34.8 psu, and potential density of 24.5 to $25.5\sigma_\theta$ is clearly seen in upper 500 db offshore from the mooring sites. The main thermocline and pycnocline become shallower in a shoreward direction (northward), with the gradient highest around the mooring sites, corresponding to the flow of the Kuroshio. At the mooring sites, the depths of the current meters deployed in the upper layer approximately correspond to the depths of the main thermocline and pycnocline. Weak salinity minimums observed below these meters are considered to have extended from NPIW in the subtropical gyre, generally above the depths of the current meters deployed in the intermediate layer. The potential densities recorded in the upper, intermediate, and lower layers were approximately $26.0\text{--}26.5$, $27.1\text{--}27.3$, and $27.4\text{--}27.5\sigma_\theta$ for, respectively.

[17] The 15°C isotherm at 200 m depth, a quantitative indicator of the axis of the Kuroshio [Kawai, 1969], was observed near the mooring sites. The estimated position of the axis was located slightly inshore of the mooring sites in April 2003 (Figures 4a to 4c), moved offshore of the sites in June (Figures 4d to 4f), and returned inshore of the sites in October (Figures 4g to 4i). According to the comprehensive

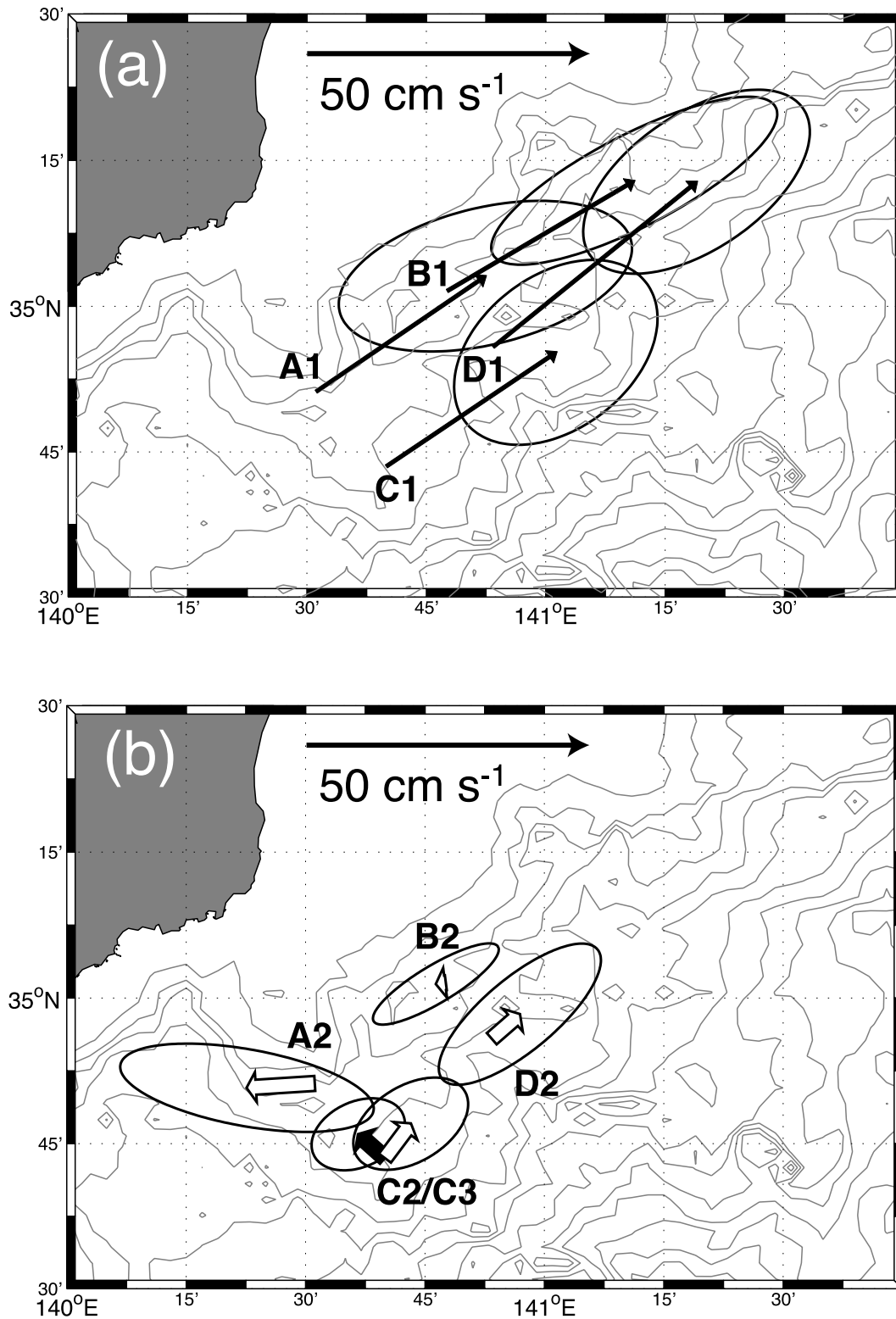


Figure 3. Mean velocity vectors and standard deviation ellipses of (a) the upper layer and (b) the intermediate (open arrows) and lower layers (shaded arrows). Start points of the vectors are drawn at the corresponding mooring sites, and the centers of the ellipses are drawn at the end points of the vectors. The contour interval for isobaths is 500 m.

Table 2. Statistics of the Processed Velocity Records^a

CM	T (d)	D (db)	\bar{V} (cm s ⁻¹)	$\bar{\theta}$ (deg)	σ_1 (cm s ⁻¹)	σ_2 (cm s ⁻¹)	θ (deg)	$\sqrt{\sigma_1\sigma_2/(\nu_1\nu_2)^{1/4}}$
A1	261	328	35.2	56	25.8	11.7	76	2.6
B1	325	328	37.2	60	27.3	7.8	63	3.1
C1	121	328	35.1	56	19.6	13.2	52	3.3
D1	326	328	45.0	51	22.2	11.6	56	2.7
A2	261	757	11.7	266	22.1	6.7	280	2.2
B2	325	757	1.7	262	12.4	3.2	239	1.1
C2	121	757	7.4	37	10.9	6.6	58	1.7
D2	326	757	6.4	49	17.4	6.3	50	2.3
C3	324	1245	6.2	312	8.4	5.6	66	1.2

^a T , D , \bar{V} , $\bar{\theta}$, σ_1 , σ_2 , θ , ν_1 , and ν_2 indicate the available period, depth, magnitude, and orientation of mean velocity, major and minor axis components of standard deviations, orientation of the major axis, and effective degrees of freedom for the t distribution for the two velocity components, calculated using the integral timescale [Emery and Thomson, 2001], respectively. See also Figure 3.

monitoring of the Kuroshio carried out by the Japan Coast Guard [Japan Coast Guard, 2003, 2004], the surface axis of the Kuroshio was generally located between 20 and 60 nautical miles (between 37 and 111 km) southwest of Cape Nojima-zaki during the observation period, while the mooring sites were located between 45 and 65 km southwest of the Boso peninsula. It is therefore inferred that the axis of the Kuroshio was located around or slightly offshore the mooring sites on average. This is consistent with a time series of the latitude of the 15°C isotherm at 200 m depth for the 33 years from 1972 to 2004 (Figure 5).

3.2. Extended EOFs

[18] The spatiotemporal structures measured by the six current meters and considering time lags of up to 50 days are decomposed into 612 extended EOFs. The top 22 functions are significant at the 95% level according to Selection Rule N [Preisendorfer, 1988], and among them explain 74% of the total variance. Figure 6 shows the first eight EEOFs. The velocity vectors of the EEOFs exhibit counter-clockwise rotation with increasing time lags, and the phases of those at site A precede those at sites B and D, implying downstream (eastward) propagation. The propagations are highly periodic, with apparently dominant periods of 15–20 days for EEOFs 1–4 and 10–15 days for EEOFs 5–8. The variance conserving power spectral density (VCPSD) of the time coefficients (scores) reveals that the most energetic periods occurred within 16–18 day bands for EEOFs 1–4 and 11–14 day bands for EEOFs 5–8, whereas moderate energy periods ranged over 20–40 day bands (Figure 7). In general, the occurrence of two EEOFs with similar periods and variance but different phase is indicative of propagation [Miller, 1997]; however, it appears that the combination of these major and minor periods requires four EEOFs. The dominant periods of the remaining 14 significant EEOFs, estimated as above, are 6–15 days, with 8 showing spatially correlated downstream propagation. The characteristics of these 16 EEOFs, which explain 67% of the total variance, are described below.

[19] Cross-correlations among six time-lag series of velocity vectors $U_{i,\delta,k}$ and $V_{i,\delta,k}$ (0- to 50-day lags for 3 sites \times 2 layers, which are part of EEOF structures) for each EEOF are calculated to estimate the spatial phase lags. Because horizontal correlations are generally stronger in the upper layer than in the intermediate layer, the time lags of A1–B1 and A1–D1 are used to examine horizontal phase structure. Vertical structure is examined via cross-

correlation between A1 and A2. With the requirement that the maximum cross-correlation coefficients of A1–B1 and A1–D1 are significant at the 99% level, we obtained 16 (EEOFs 1–10 and 13–18) with a propagating structure. The lags from A1 to B1 are larger than those from A1 to D1, despite the shorter distance between the sites in the former case. Isophase lines estimated for these upper-layer fluctuations are oriented between 28 and 55° clockwise of the mean upper-layer flow. If the fluctuations were plain waves, propagation would be almost northward, climbing the continental shelf; however, this was not observed, at least not as a major fluctuation. We therefore assume that the waves propagate downstream along the upper layer mean flow and that the orientations of the isophase lines reflect the orientations of wavefronts (Figure 8a), a pattern commonly reported in previous studies [e.g., Kimura and Sugimoto, 1993]. Because the mean field and hydrographic structure indicate that the current meters were deployed around the axis of the Kuroshio, the waves can be interpreted as downstream-propagating frontal waves, as described in previous studies [Kimura and Sugimoto, 1993; Savidge, 2004].

[20] The wavefront angle α , defined clockwise from the mean flow direction of the upper layer, has the following relationships with the site locations and the time lags of wave propagation:

$$\frac{r_{AD} \sin(\alpha - \phi_{AD})}{r_{AB} \sin(\alpha - \phi_{AB})} = \frac{\Delta T_{AD}}{\Delta T_{AB}}, \quad (7)$$

where r_{AB} and r_{AD} are the distances between site A and site B, and between site A and site D, respectively; ϕ_{AB} and ϕ_{AD} are the orientations of lines AB and AD, respectively, measured clockwise relative to the mean flow direction; and ΔT_{AB} and ΔT_{AD} are the time lags of the wave propagation between A1 and B1, and between A1 and D1, respectively (Figure 8b). If $\alpha = 90^\circ$, the wave is interpreted as a plane wave. Because the first four of the above parameters are

Table 3. Means and Standard Errors of Mean-to-Eddy Barotropic (BT) and Baroclinic (BC) Energy Conversion Rates [10^{-8} m² s⁻³] for the Upper (UP) and Intermediate (IM) Layers

Layer	BT	BC
UP	-11.3 \pm 3.3	5.7 \pm 3.4
IM	-13.1 \pm 3.5	10.0 \pm 6.4

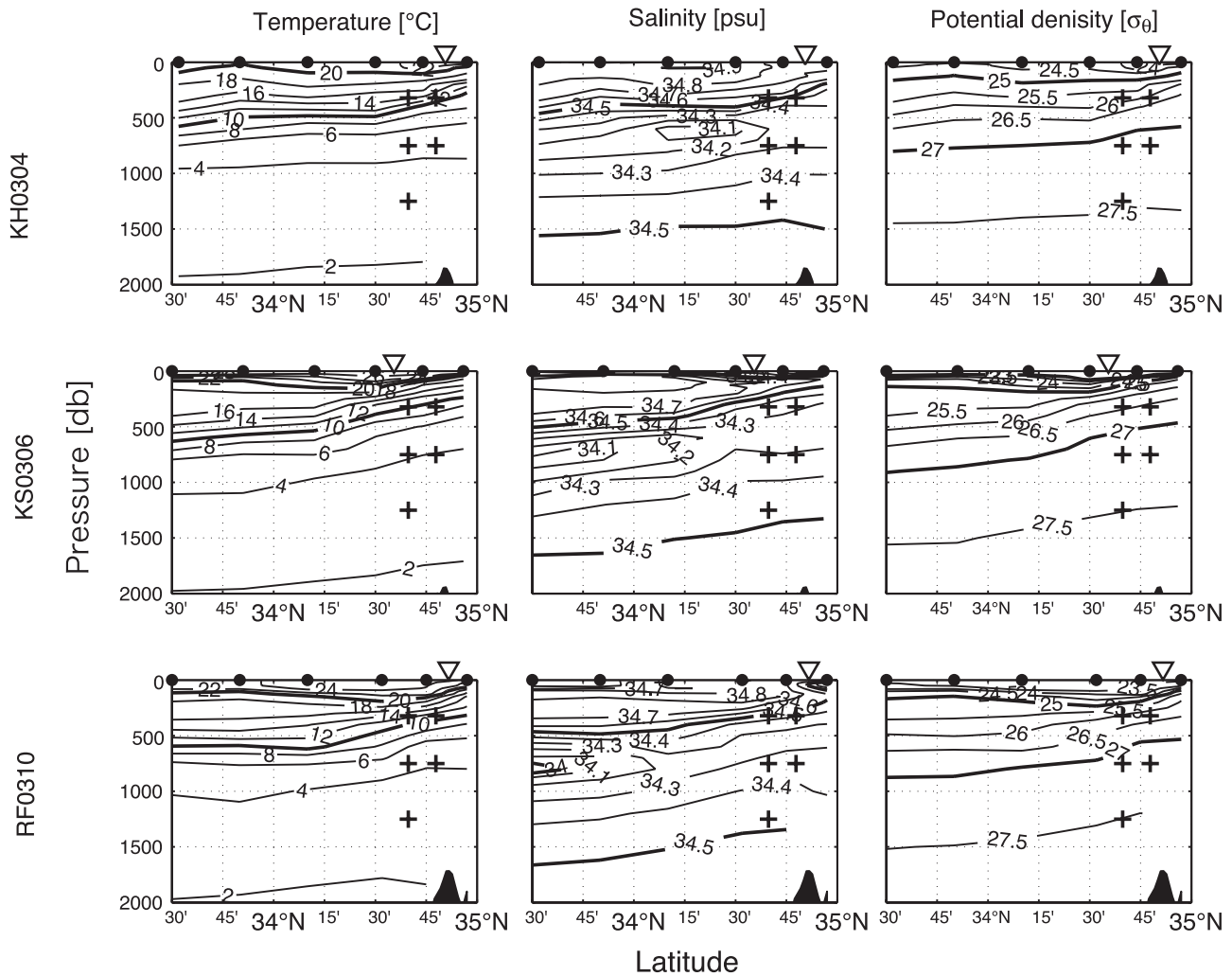


Figure 4. Hydrographic sections observed by the JMA along the PT line. (Left column) Temperature, (center) salinity, and (right column) potential density are shown. Observations during (top) April 2003 (Observation KH0304), (middle) June 2003 (KS0306), and (bottom) October 2003 (RF0310), respectively. Black circles and open triangles on the top of each figure indicate location of CTD casts and that of axis of the Kuroshio estimated with the temperature index (see text for definition), respectively. Projections of the deployed current meters are shown by crosses, and black areas in the lower parts of the figures represent bottom topography.

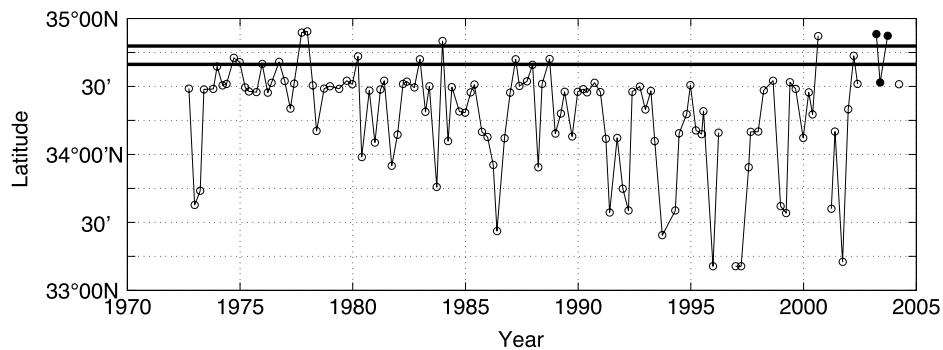


Figure 5. Latitudinal position of the axis of the Kuroshio estimated based on the temperature index (see the text for a definition of this index) using long-term records for the PT line observed by the JMA. Solid circles indicate those based on the observations in April, June, and October 2003, and thick lines are the latitudes of mooring sites projected onto the PT line.

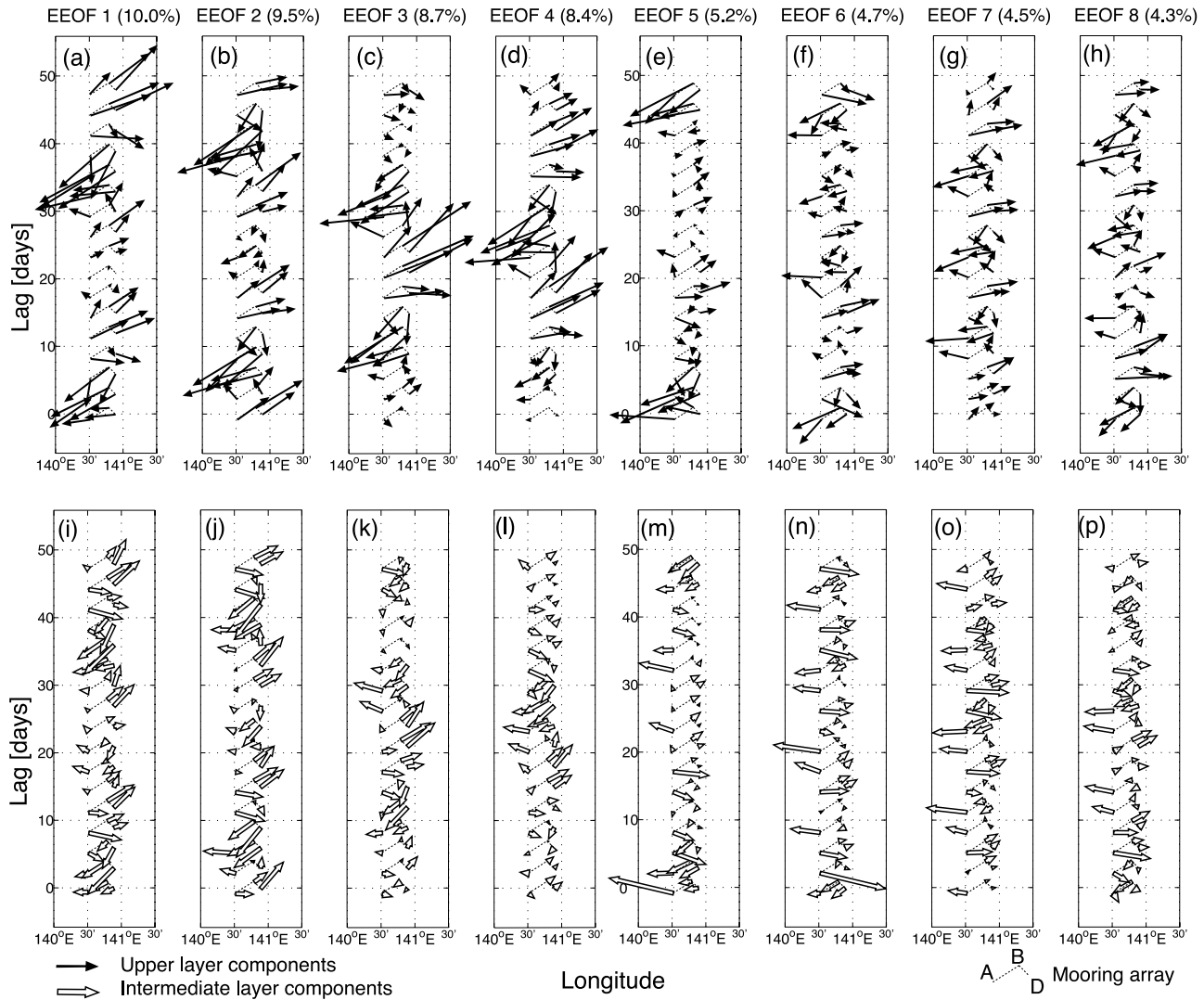


Figure 6. Structure of the first eight EEOFs for (a-h) the upper and (i-p) intermediate layers. Black and open arrows indicate the velocity vector amplitudes of the upper and intermediate layers, respectively, as drawn on rotated L-shaped broken lines that represent part of the mooring array drawn at the corresponding lag levels.

known, estimating the remaining two variables via the cross-covariance analysis method described above yields α . The along-stream distances of isophase lines from site A to sites B and D, λ_{AB} and λ_{AD} , are then defined as

$$\lambda_{AB} = x_{AB} + y_{AB} / \tan \alpha, \quad (8)$$

$$\lambda_{AD} = x_{AD} + y_{AD} / \tan \alpha, \quad (9)$$

where (x_{AB}, y_{AB}) and (x_{AD}, y_{AD}) denote the along- and cross-stream distances from site A to sites B and D, respectively. Using these values of λ_{AB} and λ_{AD} , the wave characteristics are obtained as

$$L = \lambda_{AB} T / \Delta T_{AB} = \lambda_{AD} T / \Delta T_{AD} \quad (10)$$

$$= 2\pi / K, \quad (11)$$

$$CP = 2\pi F / K = L / T, \quad (12)$$

where F , T , K , L , and C_P denote the frequency, period, downstream-wavenumber, downstream-wavelength (hereafter referred to simply as wavenumber and wavelength, respectively), and phase velocity, respectively. The vertical phase lags of the two layers are calculated from the time lag of A1 and A2 as follows:

$$\Delta\theta_{12} = \Delta T_{A1A2} / T_A. \quad (13)$$

[21] On the basis of the contribution sequence, dominant period, and phase structure, the above 16 EEOFs are assigned into 5 groups of frontal waves (I–V). Dispersion diagrams and the downstream growth rates for these waves are shown in Figure 9 and summarized in Table 4. The waves propagate downstream with periods, wavelengths, and phase velocities of 7–18 days, 220–380 km, and 22–

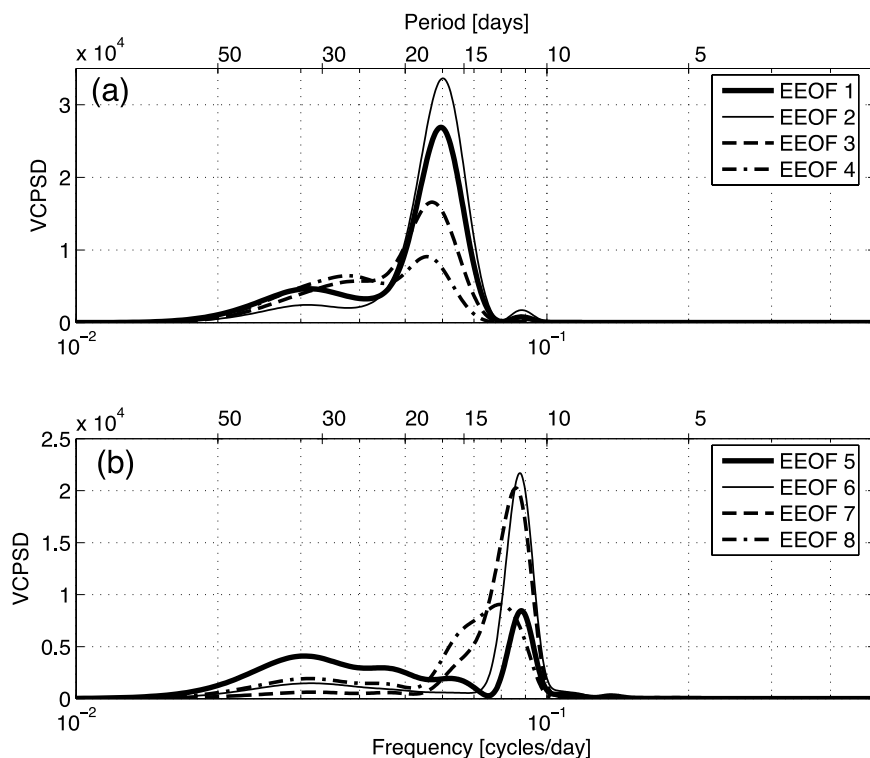


Figure 7. Variance preserving power spectra density (vcpsd) for the time coefficients of (a) EEOFs 1–4 and (b) EEOFs 5–8.

30 cm s⁻¹, respectively. The phase velocities are eastward, smaller than the mean flow velocity of about 35–40 cm s⁻¹, and larger than the mean flow at the intermediate depth of about 2–12 cm s⁻¹. The phase velocity increase with increasing frequency (period decreases) or wavenumber (wavelength decreases), as described previously in the East China Sea [James *et al.*, 1999] and the Gulf Stream region [Watts and Johns, 1982; Tracey and Watts, 1986; Savidge, 2004]. Group I waves, which contributes to 37% to the total variance, has the largest wavelength and longest period among fluctuations with periods less than 50 days. Downstream growth rates are generally higher for waves with longer periods (larger waves) (Figure 9c). Only the growth rates for Group I waves are greater than zero; the amplitudes of these waves increase downstream, whereas those for other waves decay.

[22] Figure 10 shows the structure and barotropic energy conversion rates of wave Groups I–V. The mean vertical phase lags between the upper and intermediate layers of the four main groups of waves (correlations were not significant for Group V waves) range between -0.04 and 0.12π (positive values indicate that the upper layer lags behind the intermediate layer). The lag of the Group I waves is about 0.12π ($1/8 \pi$), larger than the lag of about 0.02π of the Group II waves. The mean wavefront angles measured clockwise from the mean flow direction of the upper layer vary between 29 and 52°, with larger angles for Group I waves than for Group II. The barotropic energy conversion rates are calculated for Groups I–V in the same manner as that employed for the total velocity field. Eddy flux terms such as $u'u'$ in equation (1) are calculated by averaging $3 \times$

51 EEOF components for each layer. We found that Groups I–V convert eddy kinetic energy to mean kinetic energy in both the upper and intermediate layers. The total conversion rates of the two layers determined based on the velocity time series (after conducting a 50 day high-pass filter) are -7.55 and $-9.27 \times 10^{-8} \text{ m}^2 \text{ s}^{-3}$, respectively, meaning

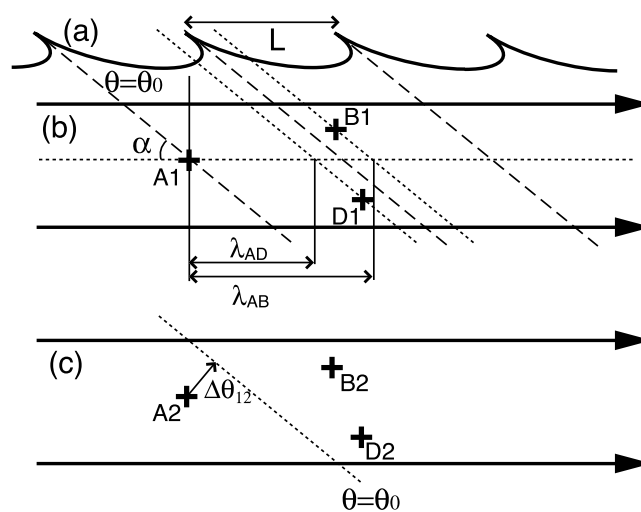


Figure 8. (a) Schematic illustrations of wave fronts. (b) Structure of wave propagation for the upper layers. (c) Structure of wave propagation for the intermediate layers. Pairs of thick, parallel arrows indicate the propagation direction, which is the same as the mean flow direction of the upper layer. See the text for definitions of parameters.

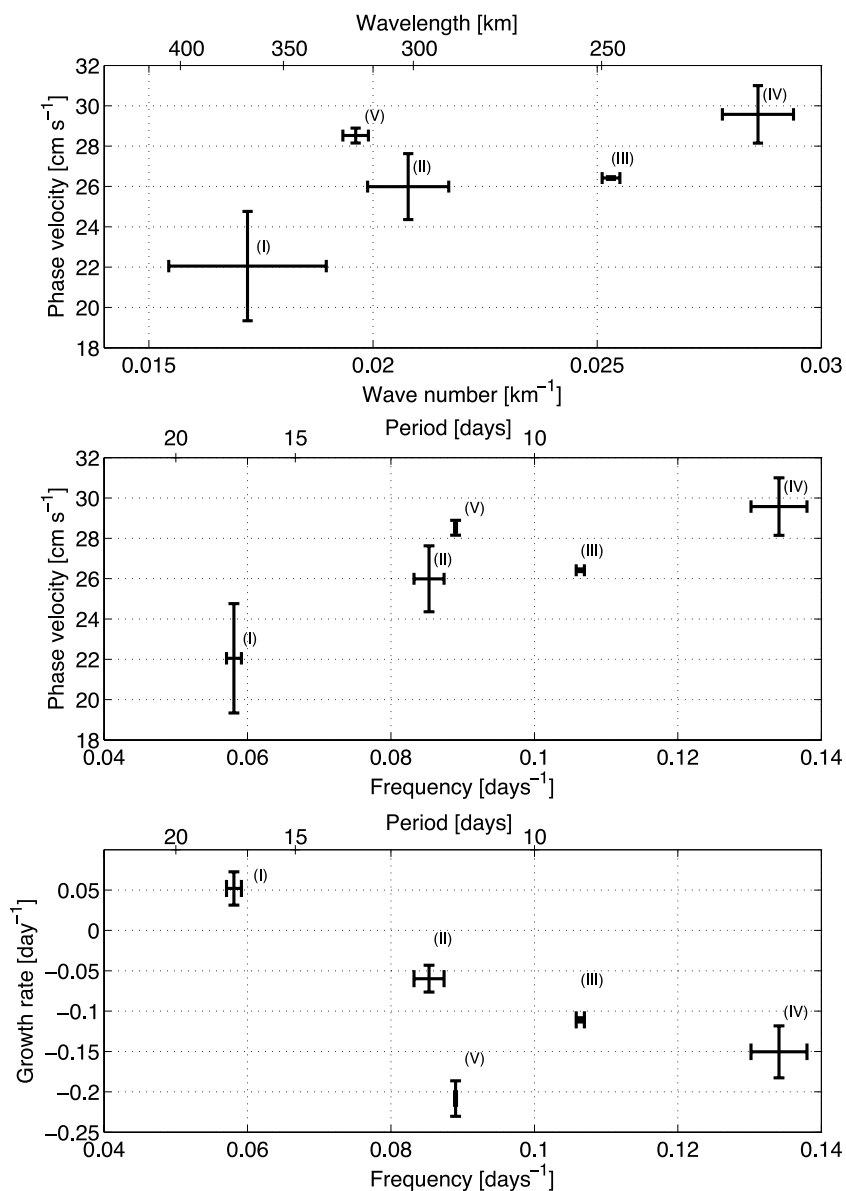


Figure 9. Dispersion diagrams and growth rates for the five wave groups (I–V): (a) wavenumber (wavelength) and phase velocity, (b) frequency (period) and phase velocity, and (c) frequency and growth rates. Error bars indicate half standard deviations among the groups.

that the conversion rates of all wave groups make similar contributions to the total variance; however, the layer in which the greatest conversion occurs is different between the two strongest wave groups, being the upper layer for Group I and the intermediate layer for Group II.

4. Discussion

[23] Downstream-propagating frontal waves are detected as significant EEOFs from the records of current meters deployed near the separation point of the Kuroshio. The recorded periods, wavelengths, and phase velocities are in the ranges of 7–18 days, 220–380 km, and 22–30 cm s⁻¹, respectively, similar to values reported for the East China Sea and areas south of Japan [Sugimoto *et al.*, 1988; Qiu *et al.*, 1990, Kimura and Sugimoto, 1993; James *et al.*, 1999].

The phase velocity is lower than the mean flow of the upper layer. Figure 11 shows a dispersion diagram of waves obtained in the present study and previous studies for the Kuroshio current system [James *et al.*, 1999; Kimura and Sugimoto, 1993; Kouketsu *et al.*, 2007] and for the Gulf Stream [Brooks and Bane, 1981; Lee and Atkinson, 1983; Tracey and Watts, 1986; Savidge, 2004]. In the Kuroshio current system, the characteristics of the waves around the separation point observed in the present study, especially those of the Group I waves (EEOFs 1–4), are more similar to those observed in an area south of Japan [Kimura and Sugimoto, 1993] than those reported from the East China Sea [James *et al.*, 1999]. In the East China Sea, the typical wavelength is smaller than those recorded at the separation point of the Kuroshio, and the phase velocity of similar wavenumber bands are slightly lower, yet in both areas the

Table 4. Propagation and Growth Characteristics (Sum or Means \pm Standard Deviations Among the Groups) of Waves I–V^a

	EEOF	Var (%)	T (d)	L (km)	C_p (cm s ⁻¹)	σ (d ⁻¹)
I	1–4	37	17.2 \pm 0.6	378 \pm 81	22 \pm 5.4	0.05 \pm 0.04
II	5–8	19	11.7 \pm 0.6	304 \pm 27	26 \pm 3.3	-0.06 \pm 0.03
III	9–10	4	9.4 \pm 0.1	248 \pm 12	26 \pm 1.3	-0.11 \pm 0.01
IV	13–16	6	7.5 \pm 0.5	220 \pm 12	30 \pm 2.8	-0.15 \pm 0.06
V	17–18	2	11.2 \pm 0.0	320 \pm 9	29 \pm 0.7	-0.21 \pm 0.04

^aVar, T , L , C_p , and σ indicate the contribution to the total variance, period, wavelength, phase velocity, and growth rate, respectively.

phase velocity increases with decreasing period and wavelength [James et al., 1999]. For waves in the Gulf Stream region, phase velocities are higher than those in the Kuroshio area, as stated above; both regions show decreasing phase

velocity with increasing wavelength [Tracey and Watts, 1986; Savidge, 2004].

[24] The dispersion relationship obtained in the present study is more similar to that downstream of Cape Hatteras [Tracey and Watts, 1986] than the relationships obtained around and upstream of the cape [Brooks and Bane, 1981; Lee and Atkinson, 1983; Savidge, 2004]. Although waves of various scales have been observed in the Kuroshio Extension, some waves west of 145°E [Kouketsu et al., 2007] are of similar scale to those described in the present study (Figure 11). The downstream amplification of larger-scale waves documented in the present study is consistent with the findings of previous studies in this region [Bernstein and White, 1977; Kouketsu et al., 2005].

[25] The energetics of the total velocity field indicate a significant baroclinic energy conversion from the mean field to the eddy field for both the upper and intermediate layers.

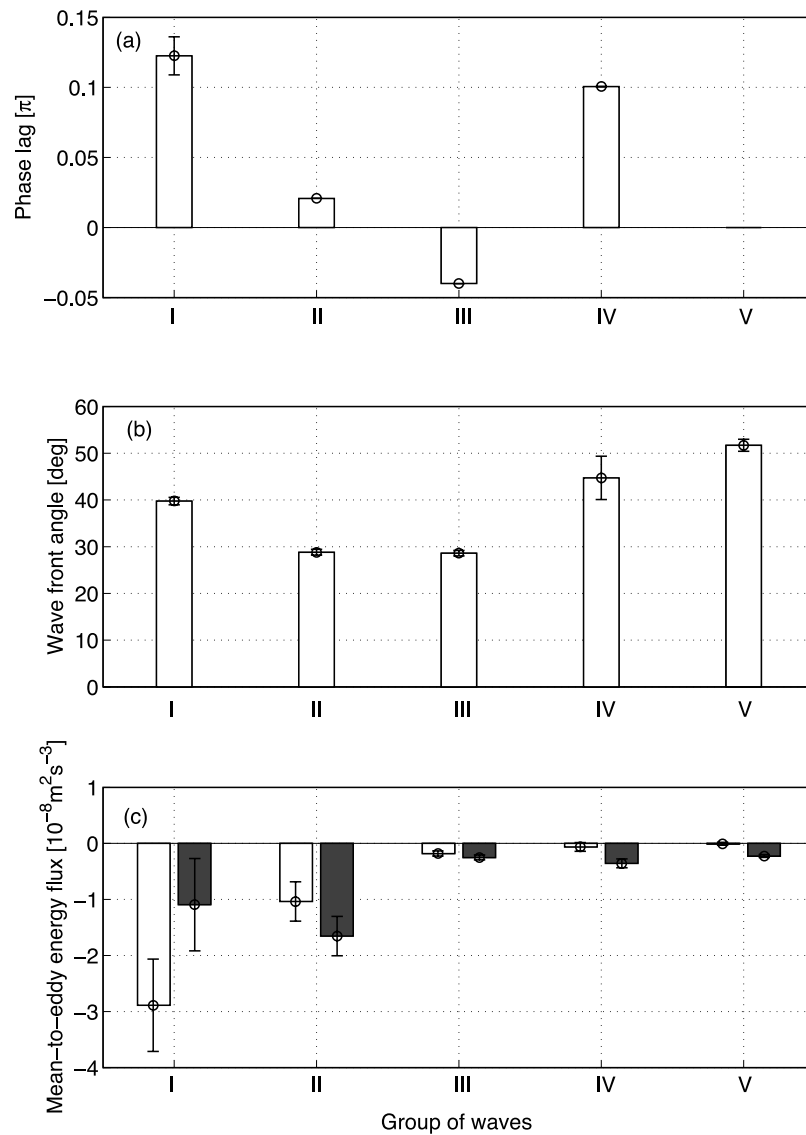


Figure 10. Structure and energetics of the five wave groups: (a) vertical phase lag, (b) wavefront angle relative to the mean flow direction of the upper layer, and (c) mean-to-eddy barotropic energy conversion rates for the upper (open bars) and intermediate (filled bars) layers. Error bars indicate half standard deviations among the groups.

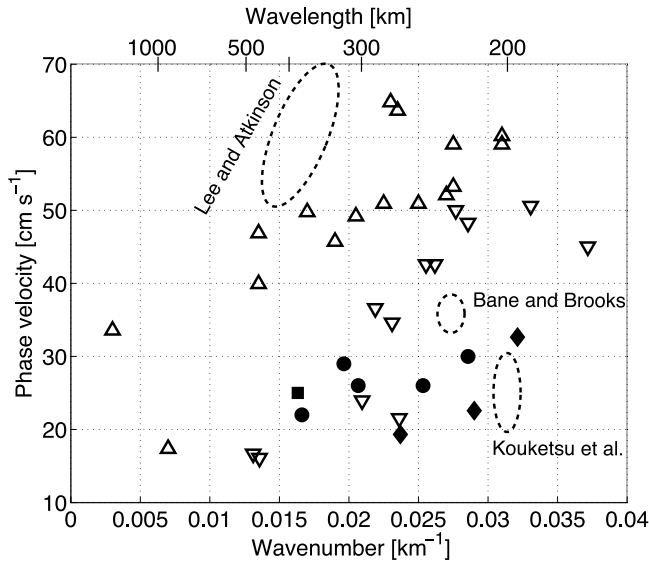


Figure 11. Dispersion diagram (wavenumber vs. phase velocity) showing data obtained in the present study and in previous studies, both in the Kuroshio and Gulf stream regions: filled circles, filled diamonds, black square, open upward triangles, and open downward triangles represent data from the present study, *James et al.* [1999] (East China Sea), *Kimura and Sugimoto* [1993] (area south of Japan), *Savidge* [2004] (Cape Hatteras), and *Tracey and Watts* [1986] (downstream of Cape Hatteras). The suggested ranges of *Brooks and Bane* [1981] (Carolina continental margin), *Lee and Atkinson* [1983] (south Atlantic Bight), and *Kouketsu et al.* [2007] (Kuroshio Extension) are shown by dashed ellipses.

Considering that the conversion in barotropic energy from the eddy field to the mean field, we assume that the eddy potential energy is converted to the eddy kinetic energy via the vertical eddy flux of density $\overline{w'\rho'}$, although direct estimations of this and other terms related to the energy budget are required for this assumption to be confirmed; such estimates cannot be made based on our mooring records. In addition to this characteristics of the energetics, the frontal waves detected by EOF analysis, especially the Group I waves, have a structure that indicates that the phase of the intermediate layer precedes that of the upper layer. We therefore conclude that baroclinic instability plays an important role in the propagation and evolution of these waves, as suggested in previous studies [*Tracey and Watts*, 1986; *Savidge*, 2004; *Kouketsu et al.*, 2007]. According to the analytical study of *Pedlosky* [1987], the downstream-propagation speed c_r of baroclinic instability waves (real part of the phase velocity) in a two-layer fluid on an f -plane, where instability occurs for some waves of small wavenumber, can be approximated as

$$c_r = \frac{U_1(K^2 + 2/R_2^2) + U_2(K^2 + 2/R_1^2)}{2(K^2 + 1/R_1^2 + 1/R_2^2)}, \quad (14)$$

where U_1 , U_2 , and K are the velocities of the upper and lower layers and the total wavenumber, respectively, and $R_i = (g'H_i)/f^2$, where H_i is the thickness of the i -th layer.

[26] Replacing R_2^2 and K with $R_2^2 = \gamma^{-1}R_1^2$ and $K' = KR_1$, using a layer thickness ratio of $\gamma = H_1/H_2$, we can simplify equation (14) as

$$c_r = \frac{U_1(K'^2 + 2\gamma) + U_2(K'^2 + 2)}{2(K'^2 + \gamma + 1)} \quad (15)$$

$$= \frac{U_1 + U_2}{2} - \frac{(1 - \gamma)(U_1 - U_2)}{2(K'^2 + \gamma + 1)}. \quad (16)$$

[27] While c_r lies between U_1 and U_2 for any K' and γ for this f -plane formulation, phase velocities of baroclinically unstable waves on the beta plane also lie between them [*Pedlosky*, 1987], which again indicates the baroclinic instability for the observed waves that propagate with a phase velocity intermediate between the mean velocities of the upper and intermediate layers. Because γ is usually less than 1, R_1 can be considered as the internal radius of deformation. Given that U_1 is usually greater than U_2 , equation (16) indicates that the phase velocity decreases as wavelength (scaled by the deformation radius) increases by a rate related to vertical velocity shear (equivalent to the horizontal density gradient in this model) and the layer thickness ratio; the upper bound of phase velocity is determined by the background flow. This trend with respect to wavelength and the upper bound is consistent with the characteristics of observed frontal waves. Using typical values measured at the present study site ($U_1 = 50 \text{ cm s}^{-1}$, $U_2 = 10 \text{ cm s}^{-1}$, $\gamma = 0.2$, $R_1 = 50 \text{ km}$, and $K = 0.017 \text{ km}^{-1}$ and $K = 0.021 \text{ km}^{-1}$ (for waves I and II, respectively)), we obtain $c_r = 21.7$ and 23.1 cm s^{-1} (for Groups I and II, respectively), which is in good agreement with the predictions of the simple model.

[28] Previous studies have proposed that the downstream phase velocity of frontal waves observed in the East China Sea is lower than those in the Gulf Stream because of a greater shelf depth and smaller volume transport [*Qiu et al.*, 1990; *James et al.*, 1999]. Although the phase velocities in these cases are lower than those in the present study (despite the shallower shelf depth in the present case), the roles of these factors seem to be related to the background velocity, layer thickness ratio, and deformation radius. Shelf depth may be related to all of these parameters either directly or indirectly, while volume transport has a direct relationship with background velocity. The trend of higher phase velocity with increased volume transport [*James et al.*, 1999] is consistent with equation (16). This trend also explains the contrasting phase speeds in the Kuroshio and the Gulf Stream, with the latter generally showing a higher velocity [*Tomczak and Godfrey*, 1993]; however, given that the two current systems show the opposite patterns of change in phase velocity (i.e., the phase velocity is higher in the upstream region of the Gulf Stream), the mechanism that explains these differences requires further observation and analysis.

[29] Although the characteristics of the observed frontal waves are well reproduced by the above model, the phase

lags are smaller than $1/2 \pi$ of the fastest-growing wave [Pedlosky, 1987]. This is first explained by the fact that the deployment depth of the upper current meter in the present study was similar to the depth of the main pycnocline, rather than above it as in the idealized two-layer model (Figure 4); this discrepancy might have led to a reduced lag difference. In addition, waves of Groups II–IV showed a relatively strong energy conversion in the intermediate layer, indicating that the background frontal structure between the northeastward Kuroshio and the southwestward coastal currents in the intermediate layer exerts a greater influence than that expressed in the simple two-layer model. While spatial correlations in the intermediate layer (about $27.2 \sigma_\theta$) are generally weaker than those in the upper layer (about $26.3 \sigma_\theta$) in the present study, the amplitudes of the waves in the $26.8 \sigma_\theta$ layer in the Kuroshio Extension are larger than those in the $25.5 \sigma_\theta$ layer [Kouketsu et al., 2005].

[30] In addition to differences in phase velocity at an equivalent wavelength between the East China Sea and the present study, a downstream increase in the dominant wavelength band is also recognized for the Kuroshio. As considered in studies in the Gulf Stream [Tracey and Watts, 1986; Savidge, 2004], topographic constraints on the development of larger-scale waves appear to be relaxed in the area around the separation point; this possibility is supported by the observation of comparable wavelengths in an area where the Kuroshio temporarily diverges from the coast [Kimura and Sugimoto, 1993]. The amplification of larger-scale waves in the separation area of the Kuroshio is also supported by the obtained growth rates, which are positive only for the waves of largest wavelengths.

[31] Satellite altimetric measurements revealed that the distribution of high eddy kinetic energy associated with synoptic-scale path variability and eddy shedding extends close to the date line [Qiu et al., 1991; Qiu, 1995]. Hurlburt et al. [1996] demonstrated that numerical models with a resolution greater than $1/16$ degree are required to reproduce this penetration. The results of the present study suggest that eddy-to-mean kinetic energy conversion and the cascading up of frontal waves are related to this process mainly via baroclinic instability, which is not always reproduced in models with coarse resolution.

[32] **Acknowledgments.** The authors are grateful to officers and crews of R/V *Tansei Maru* and *Hakuho Maru*, Mr. H. Nagae of Ocean Research Institute, The University of Tokyo, and other scientists on board, for their help in the deployment and recovery of the mooring systems. Data of seasonal hydrographic observations along the PT line are provided by Japan Meteorological Agency. The authors are also thank Dr. A. Nagano of Japan Agency for Marine-Earth-Science and Technology, Dr. I. Yasuda of The University of Tokyo, and two anonymous reviewers for their helpful comments.

References

- Bernstein, R. L., and W. B. White (1977), Zonal variability in distribution of eddy energy in mid-latitude North Pacific Ocean, *J. Phys. Oceanogr.*, **7**, 123–126.
- Brooks, D. A., and J. M. Bane (1981), Gulf-stream fluctuations and meanders over the Onslow Bay upper continental-slope, *J. Phys. Oceanogr.*, **11**, 247–256.
- Brooks, I. H., and P. P. Niiler (1977), Energetics of Florida current, *J. Mar. Res.*, **35**, 163–191.
- Dewar, W. K., and J. M. Bane (1989), Gulf-stream dynamics. part II: Eddy energetics at 73w, *J. Phys. Oceanogr.*, **19**, 1574–1587.
- Emery, J. D., and R. E. Thomson (2001), *Data Analysis Methods in Physical Oceanography*, 2nd rev. ed., 638 pp., Elsevier Science, Amsterdam, Netherlands.
- Feng, M., H. Mitsudera, and Y. Yoshikawa (2000), Structure and variability of the Kuroshio current in Tokara Strait, *J. Phys. Oceanogr.*, **30**, 2257–2276.
- Hurlburt, H. E., A. J. Wallcraft, W. J. Schmitz, P. J. Hogan, and E. J. Metzger (1996), Dynamics of the Kuroshio/Oyashio current system using eddy-resolving models of the North Pacific Ocean, *J. Geophys. Res.*, **101**(C1), 941–976.
- James, C., M. Wimbush, and H. Ichikawa (1999), Kuroshio meanders in the East China Sea, *J. Phys. Oceanogr.*, **29**, 259–272.
- Japan Coast Guard (2003), Quick bulletin of ocean conditions, No. 14 to No. 51.
- Japan Coast Guard (2004), Quick bulletin of ocean conditions, No. 1 to No. 14.
- Japan Meteorological Agency (2005), *Extreme Weather Report 2005*, 341 pp., Printing Bureau, Ministry of Finance, Tokyo, Japan.
- Kaihatu, J. M., R. A. Handler, G. O. Marmorino, and L. K. Shay (1998), Empirical orthogonal function analysis of ocean surface currents using complex and real-vector methods, *J. Atmos. Ocean. Tech.*, **15**, 927–941.
- Kasai, A., S. Kimura, and T. Sugimoto (1993), Warm water intrusion from the Kuroshio into the coastal areas south of Japan, *J. Oceanogr.*, **49**, 607–624.
- Kawai, H. (1969), Statistical estimation of isotherms indicative of Kuroshio axis, *Deep-Sea Res.*, **5**, 109–115.
- Kawai, H. (1972), Hydrography of the Kuroshio Extension, in *Kuroshio*, edited by H. Stommel, and K. Yoshida, 517 pp., Univ. of Tokyo Press, Tokyo, Japan.
- Kimura, S., and T. Sugimoto (1993), Short-period fluctuations in meander of the Kuroshio path off Cape Shiono-misaki, *J. Geophys. Res.*, **98**(C2), 2407–2418.
- Kimura, S., and T. Sugimoto (2000), Two processes by which short-period fluctuations in the meander of the Kuroshio affect its countercurrent, *Deep-Sea Res.*, **47**, 745–754.
- Kimura, S., A. Kasai, H. Nakata, T. Sugimoto, J. H. Simpson, and J. V. S. Cheok (1997), Biological productivity of meso-scale eddies caused by frontal disturbances in the Kuroshio, *ICES J. Mar. Sci.*, **54**, 179–192.
- Kouketsu, S., I. Yasuda, and Y. Hiroe (2005), Observation of frontal waves and associated salinity minimum formation along the Kuroshio Extension, *J. Geophys. Res.*, **110**, C08011, doi:10.1029/2004JC002862.
- Kouketsu, S., I. Yasuda, and Y. Hiroe (2007), Three-dimensional structure of frontal waves and associated salinity minimum formation along the Kuroshio Extension, *J. Phys. Oceanogr.*, **37**, 644–656.
- Lee, T. N., and L. P. Atkinson (1983), Low-frequency current and temperature variability from gulf-stream frontal eddies and atmospheric forcing along the southeast United States outer continental-shelf, *J. Geophys. Res.*, **88**(C8), 4541–4567.
- Miller, R. L. (1997), Tropical thermostats and low cloud cover, *J. Clim.*, **10**, 409–440.
- Mizuno, K., and W. B. White (1983), Annual and interannual variability in the Kuroshio current system, *J. Phys. Oceanogr.*, **13**, 1847–1867.
- Nagano, A., and M. Kawabe (2005), Coastal disturbance in sea level propagating along the south coast of Japan and its impact on the Kuroshio, *J. Oceanogr.*, **61**, 885–903.
- Pedlosky, J. (1987), *Geophysical Fluid Dynamics*, 2nd ed., 710 pp., Springer-Verlag, New York.
- Preisendorfer, R. W. (1988), *Principal Component Analysis in Meteorology and Oceanography*, 425 pp., Elsevier Science, Amsterdam, Netherlands.
- Qiu, B. (1995), Variability and energetics of the Kuroshio Extension and its recirculation gyre from the first 2-year topex data, *J. Phys. Oceanogr.*, **25**, 1827–1842.
- Qiu, B., T. Toda, and N. Imasato (1990), On Kuroshio front fluctuations in the East China Sea using satellite and in situ observational data, *J. Geophys. Res.*, **95**(C10), 18,191–18,204.
- Qiu, B., K. A. Kelly, and T. M. Joyce (1991), Mean flow and variability in the Kuroshio Extension from GEOSAT altimetry data, *J. Geophys. Res.*, **96**(C10), 18,491–18,507.
- Savidge, D. K. (2004), Gulf stream meander propagation past Cape Hatteras, *J. Phys. Oceanogr.*, **34**, 2073–2085.
- Sugimoto, T., S. Kimura, and K. Miyaji (1988), Meander of the Kuroshio front and current variability in the East China Sea, *J. Oceanogr. Soc. Japan*, **44**, 125–135.
- Tatebe, H., and I. Yasuda (2001), Seasonal axis migration of the upstream Kuroshio Extension associated with standing oscillations, *J. Geophys. Res.*, **106**(C8), 16,685–16,692.
- Tomcak, M., and J. S. Godfrey (1993), *Regional Oceanography: An Introduction*, 354 pp., Pergamon Press, Oxford, U.K.

- Tracey, K. L., and D. R. Watts (1986), On gulf-stream meander characteristics near Cape Hatteras, *J. Geophys. Res.*, *91*(C6), 7587–7602.
- Watts, D. R., and W. E. Johns (1982), Gulf-stream meanders: Observations on propagation and growth, *J. Geophys. Res.*, *87*(C12), 9467–9476.
- Weare, B. C., and J. S. Nussstrom (1982), Examples of extended empirical orthogonal function analyses, *Mon. Weather Rev.*, *110*, 481–485.
- Welch, P. D. (1967), The use of fast Fourier transform for the estimation of power spectra: A method based on time averaging over short, modified periodograms, *IEEE Trans. Audio Electroacoust.*, *15*, 70–73.
- Yanagi, T., T. Shimizu, and H. J. Lie (1998), Detailed structure of the Kuroshio frontal eddy along the shelf edge of the East China Sea, *Cont. Shelf Res.*, *18*, 1039–1056.
-
- S. Itoh, Fisheries Environmental Oceanography Group, Ocean Research Institute, University of Tokyo, 1-15-1 Minamidai, Nakano-ku, Tokyo 164-8639, Japan. (itohsach@ori.u-tokyo.ac.jp)
- T. Sugimoto, Ocean Research Institute, School of Marine Science and Technology, Tokai University, 3-20-1 Shimizu Ordo, Shizuoka 424-8610, Japan.